Energy Conversion and Management 319 (2024) 118866

Contents lists available at ScienceDirect

Energy Conversion and Management

journal homepage: www.elsevier.com/locate/enconman

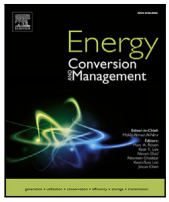

Research paper

Photovoltaic modules fault detection, power output, and parameter estimation: A deep learning approach based on electroluminescence images

Emir Ozturk [a], Emanuele Ogliari [a], Maciej Sakwa [a,*], Alberto Dolara [a], Nicola Blasuttigh [b], Alessandro Massi Pavan [b]

[a] Department of Energy, Politecnico di Milano, Milano, 20156, Italy
[b] Department of Engineering and Architecture, and Center for Energy, Environment and Transport Giacomo Ciamician, University of Trieste, Trieste, 34127, Italy

ARTICLE INFO

Keywords:
Deep learning
Photovoltaic
Electroluminescence
Fault detection
Power output estimation
Parameter estimation

ABSTRACT

Accurately detecting faults in photovoltaic modules/cells and estimating their effective power output and parameters of the equivalent circuit representation of photovoltaic modules is becoming increasingly critical for both the reliability of associated systems and the efficiency of electricity production from renewable energy sources. Existing studies often work with datasets containing photovoltaic cells that exhibit one fault at a time, leading to the classification of photovoltaic cells with multiple faults as "mixed" faults. Moreover, factors such as cell alignment and specific fault types, collectively called "cell level features", are not considered in current studies estimating the power output of a photovoltaic module. Therefore, this paper focuses on a comprehensive deep-learning pipeline to separately detect three types of faults in photovoltaic modules/cells using electroluminescence images. Furthermore, it addresses the estimation of the output power of photovoltaic modules and the series resistance of their equivalent circuit, considering the cell-level characteristics extracted from the electroluminescence images. The proposed model demonstrates its ability to detect "black core", "crack", and "edge" faults with global accuracies of 0.93, 0.868, and 0.95, respectively. Furthermore, the proposed model estimates the power output of photovoltaic modules with a normalized mean absolute error of 0.03547 and a normalized root mean squared error of 0.04892. This outperforms the base model that relies solely on non-pre-processed detected faults and significantly larger models adept at extracting features from the electroluminescence images. Moreover, the VGG16-based model estimates the series resistance in the equivalent circuit representation of photovoltaic modules with a normalized mean absolute error of 0.04472 and a normalized root mean squared error of 0.0622.

1. Introduction

In recent years, solar Photovoltaic (PV) energy has garnered substantial attention due to the growing importance of clean energy resources. In 2022, cumulative global PV capacity reached 1185 GW, marking an increase of 510 GW in 2023, the fastest growth rate in two decades [1]. However, like all electrical systems, PV systems are not immune to failures or malfunctions that can affect their performance and safety and thus lead to undesirable energy, economic, and environmental effects. The decrease in energy production from PV failures directly affects the overall electricity production of PV systems, leading to a reduction in energy yield and potentially affecting financial returns on investment. This can be a challenge for system owners, including residential users, businesses, and grid operators, as it can prolong the payback period and decrease the revenues of grid-connected systems [2]. In their lifetime, defects in PV systems can arise from several sources such as installation, degradation and environmental factors [3]. As reported in [4], PV modules can exhibit up to 17 types of defects or failures which may significantly impact the reliable operation of the entire PV system. For instance, the shunt resistance (R_{SH}) of PV modules with cracked cells can fluctuate by up to ±10%, leading to non-uniform thermal stress due to the presence of cracks [5]. Furthermore, in [6], the potential power loss in PV modules is attributed to cell cracks. In this context, black core areas in electroluminescence (EL) PV images are also related to a serious internal fault within the solar cell. These typically represent regions of localized damage within the cell, which no longer allows or reduces electron generation. This underlines the critical role of fault detection not only to preserve the efficiency and longevity of photovoltaic modules but also to ensure the reliability and sustainability of solar energy systems as a whole.

* Corresponding author.
E-mail address: maciej.sakwa@polimi.it (M. Sakwa).

https://doi.org/10.1016/j.enconman.2024.118866
Received 8 April 2024; Received in revised form 1 July 2024; Accepted 29 July 2024
Available online 22 August 2024

1.1. Defects in PV modules

PV modules play a pivotal role in harnessing solar energy for sustainable power generation. However, they are prone to various defects and faults that impact their performance. As mentioned in [4], the main reason of occurrence faults in PV modules and cells is degradation over time. The degradation due to outdoor operation is primarily affected by four factors:

1. Irradiation: solar radiation exposes PV modules to varying levels of solar energy. Over time, it may lead to anomalies such as discoloration.
2. Temperature: fluctuations in temperature impact material properties. Thermal stress can cause breakages and frame damage.
3. Humidity: moisture infiltration due to humidity can lead to snail trails, interconnection issues, and cell deterioration.
4. MechanicallLoads: mechanical stress from wind, snow, or handling can result in edge defects (dark gray spots near the edges) and structural failures.

Furthermore, it is important to recognize that these defects are closely related and may influence each other, thus increasing the likelihood of coexisting and triggering a chain reaction. In addition to the outdoor operation, defects could occur during the manufacturing process, transportation, handling, and installation of PV systems as well [4]. To illustrate, in [7], researchers have observed with an experimental setup that vertical transports have a lower impact on cell cracks than horizontal transports.

On the other hand, not all defects have an immediate negative impact on performance. For instance, thin dark rectangular regions (finger failures) in solar cells may not significantly affect initial cell output [4]. However, some of the defects might lead to serious consequences. For example, one of the significant effects of cell cracks is black cores which affect the PV module's performance negatively and can only be seen with special techniques such as EL imaging. This is because cracks allow water to enter inside PV cells and due to corrosion inside, PV cells deteriorate over time. This deterioration may not be seen through the naked eye and the PV module could be missed during the inspection process.

1.2. Inspection methods of PV modules

From a broad perspective, several popular defect detection methods are employed in the field of photovoltaics. These methods include I–V curve tracing, visual inspection, infrared (IR) thermography, and various imaging techniques such as EL, photoluminescence (PL), and ultraviolet (UV) fluorescence [8]. The I–V curve tracing method facilitates anomaly detection by considering the short-circuit and open-circuit conditions of a PV module [9]. However, this method does not provide a comprehensive individual component analysis, limiting the classification of defects to a relatively small number of classes such as by-pass diode failures, corrosion, delamination, and degradation [8]. In [10], researchers have also explored the correlation between defects and the I–V curve. Nevertheless, the complex impact of cracks on power measurements has significantly reduced the accuracy of defect classification.

IR thermography relies on temperature-based measurements and it is one of the non-destructive measurement methods, that has been widely used to detect defects in PV modules. In IR imaging, infrared rays that are emitted from PV modules are captured by infrared cameras [4]. In [11], researchers have focused on detecting defects and soiling loss in PV modules. Also, a low-cost embedded method for the detection of 5-class faults through IR thermography was investigated and developed in [12]. However, IR imaging is limited by the conditions in which the measurements are taken, and not all the defects/failures of PV modules result in a temperature increase [13].

EL imaging stands out as a non-destructive method that provides high-resolution images, allowing for efficient analysis and labeling within 10–30 s. The imaging process is carried out in a dark environment by an exciting PV module with an external power supply and recording the image with CCD cameras [14]. Alternatively, easier and cheaper, an RGB digital camera could be used with a modification [15]. By using EL, defects on the PV module appear as dark regions and lines [14]. EL imaging enables the detection of anomalies within individual cells even at material structure level [13]. Notably, it can identify developing faults that might otherwise go unnoticed during routine inspections. EL image-based methods have been used by many researchers to detect defects with machine learning (ML) algorithms in PV modules and cells due to an increase in publicly available data, specifically, the dataset used in [16].

PL imaging shares similarities with EL imaging, but also exhibits distinct features. With this technique, PV modules are excited through illumination and there is no need for an external power source as opposed to EL. Hence, unlike EL, PL does not require an electrical bias; instead, it relies on the absorption of light to generate luminescence. However, in [17], researchers have mentioned that PL should be turned into a high throughput method for outdoor measurements with an artificial light source, and to minimize the sun's background noise, recordings have been made at night. Hence, in [17], recorded PL images outdoors with an artificial light source at night. It has been shown that PL imaging is also well-suited for various types of defects in PV modules. For inactive areas, EL imaging has performed better than PL imaging and interconnection failures have not been detected by PL imaging because of the excitation character of PL as opposed to EL. However, for ethylene-vinyl acetate (EVA) degradation is not visible in EL.

1.3. Defect detection and machine learning

As ML algorithms have become increasingly reliable and fast, researchers have shifted their focus toward processes that can reduce extensive labor work and leverage accumulated experience. Specifically, previous studies have demonstrated that the combination of Computer Vision (CV) and ML holds strong potential for analyzing images of PV modules and cells to detect faults [18–21]. In particular, [18] proposed an automatic classification system for IR images of PV modules based on Convolutional Neural Networks (CNNs) where they obtain an average accuracy of 99% in a binary classification problem. Similarly, an automatic system to perform fault detection and classification based on IR and RGB images on a large-scale PV system is proposed in [19] where an average accuracy of more than 99% is achieved for an 8-class problem. However, research is also focusing on real-time embedded ML classification of images on microprocessors (TinyML), so as to improve bandwidth, latency, economics, reliability, and privacy (BLERP) limitations [20]. In addition, in [21] the TinyML classification on visible images is also proposed, achieving an average accuracy of 96% for ten different defects. Moreover, a low-cost embedded hardware prototype was designed to test the ML model in real-time experiments.

To illustrate, in 2019, researchers studied CNNs on EL images to identify defective PV cells [16]. According to the results, the CNN model achieved an impressive average accuracy of 88.42%, outperforming the Support Vector Machine (SVM) model, which achieved an accuracy of 82.44% on a dataset of 2624 cell images. Building upon this foundation, other researchers have continued down the same path, developing even more robust algorithms and refining the achievements of their predecessors. This potential stems from the cumulative progress in transfer learning and feature extraction techniques, including models such as AlexNet [22], VGG [23], ResNET [24] and YOLO [25].

1.4. Related work

1.4.1. EL image based fault classification and detection studies

In [16], the applicability of CNNs on EL images to determine defective PV module cells has been studied. According to the results,

the CNN model has reached an average of 88.42% and the SVM model has achieved 82.44% accuracy on 2624 cell images. However, the model was trained to perform only binary classification (either *functional* or *defective*), not classifying the typology of the fault. In the same year, an average accuracy of 93.02% was achieved in [26] by using the same dataset proposed in [16] and implementing a Data Augmentation (DA) method. However, again, the model was solely predicting whether the cell is functional or defective. In [27], authors have proposed a Deep-feature-based (DFB) method where the features of an EL image are extracted with a Deep Neural Network (DNN) and the classification was performed with SVM. Their solution has reached an average accuracy of 90.57% and 94.52% on the dataset [16] with 4-class and 2-class classification, respectively. In another study [28], authors have combined CNN and SVM methods to classify defective cells on two different datasets, with the first dataset being the same as [16] with the same binary classification. Authors have shown that a combination of the two models has enabled their model to achieve an accuracy of 99.49% and 99.46% on the two datasets, respectively.

In another paper [29], the authors have designed an automated pipeline for EL image pre-processing and fault classification on 5400 cell images. Their pipeline takes raw EL images and crops them into cells automatically. Then, on the cell images, they utilized three different ML models. Namely, Random Forest (RF), SVM, and CNN. Among those, the CNN model has achieved the best accuracy of 99.71%. The model has classified the cells based on three different categories: *good*, *cracked*, and *corroded*. Moreover, in [30], the authors have developed an ML pipeline to extract images of cells from PV modules and classify the defects around the categories: *crack*, *oxygen*, *solder*, and *intra-cell*. Subsequently, they compared four ML models and reported that YOLO has reached an F1 score of 0.78 for object detection and ResNet18 has reached an F1 score of 0.83 for the classification.

To solve the lack of datasets regarding EL images, the authors in [31] have introduced an efficient joint data augmentation method that aims to increase the number of images by using the combination of Generative Adversarial Networks (GAN) and image alternation. They showed the effectiveness of their method by comparing it with the other existing CNN models, namely, Inception V3, VGG16, ResNET50, and MobileNet. In the most recent study [32], researchers have implemented GAN based data augmentation method on the dataset [16] to solve the data ratio imbalance on the four classes in the original dataset. Moreover, a high-resolution network (HRNet) has been used by replacing the classification layer with a self-fusion network (SefNet). As a result, the proposed model has achieved an accuracy of 94.90%, the current state-of-the-art on the dataset of [16].

In [33], the authors have used an object detection method on the EL images of PV modules. Their model has aimed to classify the images based on the categories *detect-free*, *crack*, *broken cell*, and *unsoldered area*. After the classification process, three faults have been illustrated with a bounding box around them. As a result, the proposed model based on a multichannel fusion of Faster-RCNN and R-CNN has reached a regression accuracy of 98.3% regarding fault detection and 78.86% regression accuracy of the bounding boxes. Similarly, in [34], researchers have trained a CNN to localize the top 14 types of defects out of 19 in total on PV modules and achieved a mean average precision (mAP) of 70.2%. In addition, in [35], authors have designed a model to detect faulty cells on a PV module by using object detection. The model detects the faulty cells and puts a bounding box around them but not within the cell. As a result, they have reached an average precision of 94.76% on the validation dataset with the implementation of data augmentation. However, in all three studies, the location of the faults within the cell has not been detected. On the other hand, the distinct point of the studies [33,34] is the combination of localization and classification of the faults within a PV module. Hence, the probability of multiple faults in a cell is not disregarded by definition.

In addition to object detection methods, in [36], authors have proposed an automated end-to-end anomaly detection pipeline on EL images, performing binary pixel-level segmentation. However, although their model identifies micro-cracks, cracks, dead spots, weak areas, and weak cells, segmented anomalies have not been separated into categories. In [37], researchers have automated the process of detecting and localizing the defects by using semantic segmentation, providing pixel-level localization of the defects. Their dataset consists of 17,064 annotated cell images containing 9 different defect classes, which is higher compared to existing datasets available at that time. Some of the defect classes merged into one to balance the class distributions. Therefore, four different defect classes have been used in total. Their proposed model comprised of DeepLabv3 pretrained model with a ResNET50 backbone. Their model has identified and localized non-defective areas, cracks, corrosion, contact, and interconnection defects with an average of 0.69 F1-score and achieved 95.4% pixel-level global accuracy.

Different approaches for detecting faults in PV modules and cells that were presented in this section can be summarized in Table 1, Table 2, and Table 3.

1.4.2. Image based PV module power related parameters estimation based studies

The images of PV modules can also be used to estimate the characteristic parameters of the electrical model of the module considered. In this way, it is possible to estimate the power production and the module parameters without disconnections or the usage of electrical equipment. In [6] the authors have presented an ML approach to estimate power loss in PV modules due to cell cracks. Firstly, they have created EL and I–V curve measurement datasets. Then, a statistical analysis of the cells' luminescence histogram has been performed which they have used to extract features from the EL images regarding inactive areas. As a result, with a custom non-linear regression, they have achieved R^2 of 0.869 and a maximum error of 0.17.

A DL pipeline for estimating PV power has been studied in [38]. A regression-based PV module power estimation has been performed on 719 EL images from PV modules at various stages of degradation and cell cracks. Additionally, the dataset includes 3 different types and use cases of PV modules. Namely, the T1 category with indoor and on-site, the T2 category with only on-site, and the T3 with only indoor PV modules with different brands for each category. After extraction of EL images of PV modules from on-site images, they performed feature extraction from the EL images by using SVR, and pre-trained DL models (ResNet18, ResNet50, and MobileNetV2). Therefore, they have reported that DL models perform significantly better as opposed to the baseline regression model, 7.3 ± 6.5 Wp (ResNet18) compared to 9.0 ± 8.4 Wp (SVR).

In [39], the authors examined a performance prediction of PV modules from EL images. They have introduced CNN based ML model and classified images in terms of degradation level on busbars of cells. As a result, the cells have been classified into 5 different classes with 95% accuracy. After the classification process, the correlation between EL images and I–V curve features has been analyzed. They have observed that 4 EL features were highly correlated with the I–V curve features such as R_s, V_{mp}, I_{mp}, and P_{mp}. Therefore, they have built a polynomial regression model to predict the maximum power and the series resistance in the equivalent circuit of the module. The results show that they have reached an adjusted-R^2 of 0.88 by using the median intensity and an adjusted-R^2 of 0.87 by using the fraction of the dark pixels on the degraded cells.

An inverse model to estimate solar cell images from synthetically created EL images has been proposed in the paper [40]. To train the modified VGG19-based model, the authors have created 75,000 synthetic EL images with randomized parameters of the physical model on simulation. It is reported that the CNN model has successfully learned the inverse mappings between the EL images and the physical model. Although the images have been created on the simulation, this paper demonstrates the possibility and effectiveness of DL and CNN models to predict the physical models of PV modules from the EL images.

Table 1
Classification-based studies.

Ref.	Defect Classes	Model	Metrics	Dataset
[16]	Def. or Func.	SVM	Acc: 82.44%	2,624 Cell Images
	Def. or Func.	CNN	Acc: 88.42%	2,624 Cell Images
[26]	Def. or Func.	CNN with DA	Acc: 93.02%	[16]
[27]	Def. or Func.	DFB + SVM	Acc: 94.52%	[16]
	33% Def. or 66% Def. or Def. or Func.	DFB + SVM	Acc: 90.57%	[16]
[28]	Def. or Func.	CNN + SVM	Acc: 99.49%	[16]
	Good or Corroded/Cracked	CNN + SVM	Acc: 99.46%	1,028 Cell Images
[28]	Good or Corroded or Cracked	SVM	Acc: 99.43%	5,400 Cell Images
	Good or Corroded or Cracked	RF	Acc: 97.46%	5,400 Cell Images
	Good or Corroded or Cracked	CNN	Acc: 99.71%	5,400 Cell Images
[30]	Crack or Oxygen or Solder or Intra-cell	YOLO	F1: 0.78	18,954 Module Images
	Crack or Oxygen or Solder or Intra-cell	ResNet18	F1: 0.83	18,954 Module Images
[31]	Detect-free or Micro-crack or Finger-inter. or Break	GAN	Acc: 83%	-
	Detect-free or Micro-crack or Finger-inter. or Break	VGG16	Acc: 82%	-
	Detect-free or Micro-crack or Finger-inter. or Break	ResNet50	Acc: 67%	-
[32]	Non-Def. or Poss. Normal or Poss. Def. or Def.	Sef-HRNet	Acc: 94.90%	[16]

Table 2
Object detection-based studies.

Ref.	Defect Classes	Model	Metrics	Multiple Boxes	Dataset
[33]	Broken Cell or Crack or Unsoldered	Faster-RCNN + R-FCN	Acc: 98.3%, mAP: 85.7%	Yes	1462 Module Images
	Broken Cell or Crack or Unsoldered	Faster-RCNN	Acc: 91.3%, mAP: 80.1%	Yes	1462 Module Images
	Broken Cell or Crack or Unsoldered	R-FCN	Acc: 94.7%, mAP: 82.9%	Yes	1462 Module Images
[34]	14 Different Defect Classes	Mask RCNN with ResNet-101 Backbone	mAP_{50}: 70.2%	Yes	5983 Module Images
[32]	Defect	YOLO	AP: 91.34%	No	2144 PV Module Images
	Defect	YOLO + DA	AP: 94.76%	No	2144 PV Module Images

Table 3
Segmentation-based studies.

Ref.	Defect Classes	Model	Metrics	Dataset
[36]	Defective and Non-defective Areas	Custom DNN for Segmentation	AP: 99.36%	ELPV [16] (Augmented to 2692) + TechnaliaPR (Augmented to 8722)
[37]	Non-defective or Crack or Corrosion or Contact or Interconnection Areas	DeepLabv3 with ResNet50 Backbone	F1: 0.69, Acc:95.4%	17,064 (with 256 Generated Images)

In [10] the authors focused on the prediction of 3 types of defects (cracks, corrosion, and solder failure) in the cells based on I–V curve measurements. In other words, instead of using EL images, the authors have focused on the detection of 3 types of defects from the I–V measurements of the module since in this way, classification would be faster. The importance of features of I–V curve measurements has been analyzed based on RF and XGBoost ML algorithms. Even though in this study the power-related parameters have not been predicted, they observed that defects in PV modules correlate with the I–V curve measurements. Moreover, with the inclusion of cracks among the defects, the accuracy level has decreased. As reported, this could have resulted from the complex impacts of cracks on I–V curve parameters. In this paper, although the approach is the reverse compared to [6,38–40], the correlation between I–V curve measurements and defects has been demonstrated.

2. Motivations

In the field of PV research, several studies have focused on classifying defects within PV cells by utilizing EL images. However, these investigations solely address defect classification without predicting the power output of the entire PV module and parameters in the equivalent circuit of PV modules. Furthermore, most of the existing studies aim to detect one defect at a time. In other words, existing studies often work with datasets containing PV cells exhibiting one fault at a time and PV cells with multiple faults are classified as *mixed* faults.

In addition, some studies focus on predicting the power output of the PV modules from only the EL images of PV modules. On the other hand, these studies typically overlook cell-level features, which could decrease the prediction accuracy significantly. For instance, factors such as cell alignment and specific fault types are not considered.

To the best of our knowledge, features such as how the cells aligned, or the types of faults they include have not been considered before during the estimation of the power output of a PV module. Furthermore, there is no such comprehensive study that focuses on detecting defects, estimating the power output, and series resistance of the equivalent circuit of PV modules. Hence, in this paper, a complete DL pipeline that simultaneously deals with the following concerns is introduced. The model detects faults within individual PV cells, predicts the overall power output of the PV module, and predicts the series resistance in the equivalent circuit representation of the PV module by considering cell-level features during this process. By bridging the gap between defect detection, power prediction, and parameter estimation, our research aims to spark new discussions in this field.

Summarizing, the main paper contributions are twofold:

- To the best of the authors' knowledge, the paper includes the most comprehensive deep learning pipeline which accomplishes three different tasks in two different stages. The result of the first stage is being used by the second stage. Namely, defect detection (1st stage), power output, and series resistance estimation (2nd stage).
- Due to a unique approach to cell-level features and detected faults, the model size has been decreased significantly and the performance has increased (even surpassed previously used models) in terms of power output estimation.

2.1. Objective of the research

Defects in PV modules play a critical role in the reliable operation of PV systems, making their detection a crucial area of study. Furthermore, accurate power output estimation not only ensures reliable operation but also enhances efficiency by reducing costs and preventing additional power losses. Hence, the primary objective of this paper is twofold: first, to investigate the possibility of detecting defects in photovoltaic (PV) modules using deep learning (DL) techniques. Second, to predict the power outputs and series resistances in the equivalent circuit representation of PV modules based on EL images by focusing on cell-level features.

Achieving high scores in accuracy, recall, precision, and mAP is crucial for successful defect detection. This paper is dedicated to developing the best model and optimizing these metrics. Additionally, when predicting the power output and series resistance of PV modules, minimizing the error becomes paramount. A low error rate instills trust and empowers decision-makers to take necessary actions, ensuring the reliability of associated systems.

2.2. Paper structure

In Section 3, the details regarding the dataset and PV modules will be presented as a case study. Then, In Section 4, the proposed methodology will be shared. Lastly, in Section 5, the results will be demonstrated.

3. Case study

In this section, the dataset and some specific details regarding the PV modules will be introduced that will be fundamental throughout the proposed methodology.

3.1. Dataset

The dataset is collected from a power plant located in Northern Italy, which can be seen in Fig. 1 that uses a rooftop-installed photovoltaic generator for powering farming infrastructure. Specifically, the dataset is composed of 29 ILB-Helios NA230W-P PV modules with polycrystalline cells including different typologies of defects. Across the tested modules a significant power drop has been detected due to the present defects.

Fig. 1. The PV system under investigation from which the EL images from the PV modules were captured.

Since the dataset consists of 29 PV modules made of 60 PV cells each, the total amounts to 1720 EL images of PV cells. However, since PV cells should not be considered independent from the module they belong to, EL images were grouped according to the module names in the dataset.

To determine specific details about the PV modules, modules were extracted from the plant and taken to the lab, where they were excited with an external power source at 25 °C and with a mean irradiance of 1000 W/m^2. Then, images of the PV modules were taken with a CCD camera. Furthermore, the I–V curve of the 29 PV modules was also measured to determine the maximum power point (MPP) of the PV modules.

It has been observed from the I–V curve of the PV modules that the presence of cell defects is strictly correlated with decreased power production. Some of the examples of the EL images and the I–V curves of the PV modules can be seen in Fig. 2, Fig. 3, and Fig. 4. The power output of the PV module, Fig. 2, is 230.520 W since the cells are healthy. On the other hand, the PV module, Fig. 4, has significantly more black areas in EL images, which represent the inactive areas in PV cells. Thus, the power output is 199.563 W. In addition, the PV module, Fig. 3, has fewer black areas which affected the power output positively. However, the power output, 221.985 W, is still less than the rated power, 230 W.

At this stage, it can be observed that the darker, inactive areas have an impact on the power output. However, these areas have not been distinguished yet in terms of their type. A detailed assessment of the types of defects will be performed in further sections.

3.2. Details about PV modules

3.2.1. The electrical model of PV modules

Since the cell-level features are included to enhance the accuracy of the DL models, before moving on to the proposed methodology, the details regarding the PV modules should be discussed. A PV cell can be represented by an equivalent electrical circuit. The models of a PV module are an extension of the single cell considering the adequate number of cells in series. The phenomena occurring in the PV cell can be easily represented by a current generator and a diode (three-parameter model) as well as by complex models featuring one current generator, two diodes, and two resistances (seven-parameter model). The accuracy increases with the number of parameters together with the computational load and the amount of information required to define its parameters. For the representation, in this paper, the five-parameters model was selected.

The five parameters equivalent circuit [41] is reported in Fig. 5. It includes two resistances, the light-generated current I_{PV}, and the

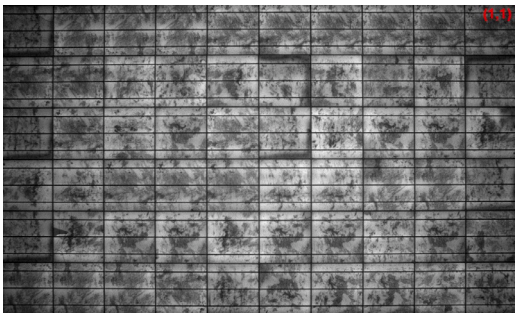

(a)

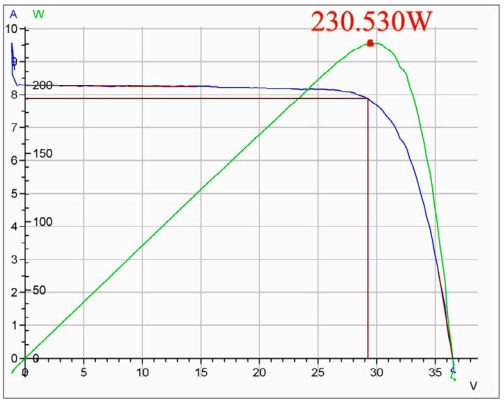

(b)

Fig. 2. The EL image (a) and I–V curve (b) of the module "10417".

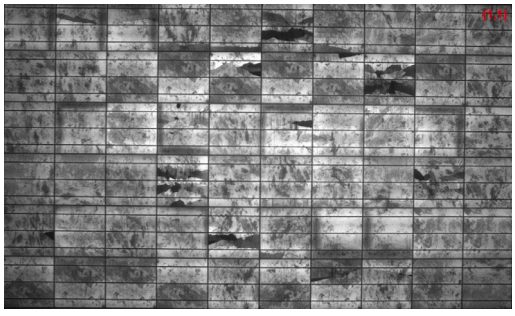

(a)

(b)

Fig. 3. The EL image (a) and I–V curve (b) of the module "10498".

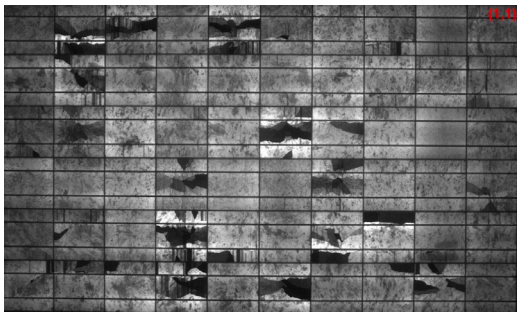

(a)

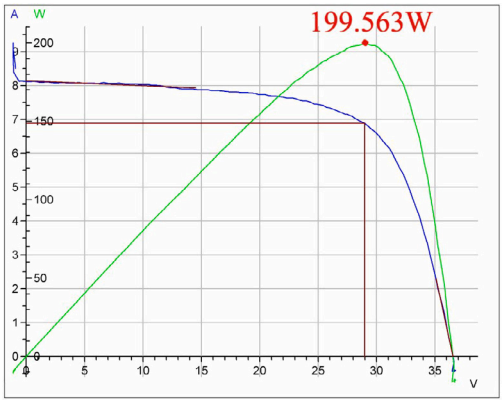

(b)

Fig. 4. The EL image (a) and I–V curve (b) of the module "14093".

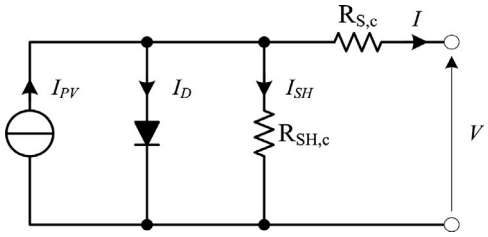

Fig. 5. 5-Parameter model.

electrical behavior of the PN junction (I_D). The cell shunt resistance $R_{SH,c}$ and the cell series resistance $R_{S,c}$ are connected in parallel to the current generator in series to the cell terminals, respectively. In particular, $R_{SH,c}$ and $R_{S,c}$ represent the recombination losses and the Ohmic losses occurring in the cell.

The five-parameter model, which is an implicit equation because of $R_{S,c}$, is described in Eq. (1) for a single PV cell.

$$I = I_{PV} - I_0 \cdot [e^{\frac{V+R_{S,c}\cdot I}{n\cdot V_t}} - 1] - \frac{V + R_{S,c}\cdot I}{R_{SH,c}} \quad (1)$$

In particular, I_0 and n represent the reverse saturation current of the pn-junction and the diode ideality factor, respectively. When moving from the single cell to a module with N_S cells in series, the previous equation becomes, Eq. (2):

$$I = I_{PV} - I_0 \cdot [e^{\frac{V+R_{S,m}\cdot I}{n\cdot N_S\cdot V_t}} - 1] - \frac{V + R_{S,m}\cdot I}{R_{SH,m}} \quad (2)$$

where $R_{S,m}$ and $R_{SH,m}$ are the overall series and shunt resistance of the module. In this paper, among the five parameters of the equivalent circuit, the series resistance ($R_{S,c}$) and the product of the current ($I =$

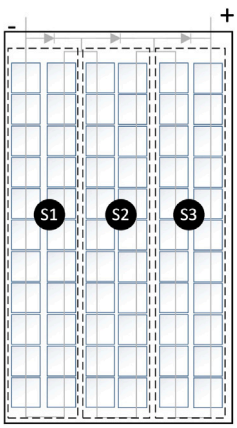

Fig. 6. Connection of PV Cells with Bypass Diodes in a PV Module.

I_{MPP}) and the voltage at MPP ($V = V_{MPP}$) will be estimated, which results in $P_{MPP} = I_{MPP} \cdot V_{MPP}$.

3.2.2. The connection of PV cells

Conventional modules, whether based on Back-Contact (BC) or Passivated Emitter Rear Cell (PERC) technology, adopt a series-connected arrangement of PV cells within each module. In the configuration, Fig. 6, multiple PV cells form a string connected to a bypass diode. Notably, each string encompasses one-third of the total PV cells in the module, covering a corresponding one-third area of the PV module's surface (S_1, S_2, S_3). In the event of shading occurring on a cell within a string, the bypass diode activates. While this prevents the shaded cell from causing a complete power loss makes the entire string inactive (for instance, S_1). This traditional setup is characterized by a proportional relationship between the number of strings and the number of bypass diodes, impacting the module's overall performance under partial shading conditions.

The string connection of PV cells in the module will be fundamental in the proposed methodology (Section 4). This information allows us to pre-process the data for the power output and series resistance estimation so that the developed DL model understands cell-level features.

4. Proposed methodology

This section will introduce the proposed methodology, providing details of the types of failures analyzed and their characteristics, the methods used to classify them, and the metrics used to assess their performance. The proposed methodology will be based on the following process: the EL images of the PV module will be separated into PV cells and defects in each cell will be labeled. The labeled data will flow into the DL pipeline, where defects in each PV cell will be detected and, by extracting the features of the PV cells, the power output and the series resistance of the equivalent circuit of the PV modules will be predicted. Finally, the results of the DL pipeline will be evaluated. The complete methodology can be seen in the flowchart in Fig. 7.

4.1. Fault types and visual assessment

In the dataset, there are three main faults in the EL images of PV cells. Namely, *black-core*, *crack*, and *edge* faults. *Black-core* faults are the black areas that are separated from the rest of the PV cell with a clear boundary. *Crack* faults are complex trails that have clear starting and ending points. It is important to point out that there is a possibility that numerous cracks are present in a single cell. Lastly, *edge* faults are the shaded areas located on the sides of the PV cell. The main difference between *edge* and *black-core* faults lies in the clearness of the boundary definition with *black-core* faults being more clear whereas the boundaries of *edge* faults are usually blurry gray areas. Some of the examples of the three types of faults can be seen in Fig. 8.

These faults were analyzed as follows:

- If there are no visible faults on the EL images, label the corresponding cell image as *empty*.
- If there are visible faults on the EL images, label the corresponding faults on the cell image as *black-core*, *crack*, or *edge* after careful assessment of the fault borders and types.

Using bounding boxes to label defects is one of the most effective ways since the ML model will learn where to look and the shapes of the objects on an image. Although this type of labeling consumes much more time compared to the classification of the image, the labels will be more precise. Hence, for *black-core* and *edge* faults bounding boxes were used. On the other hand, precise labels require consistency during

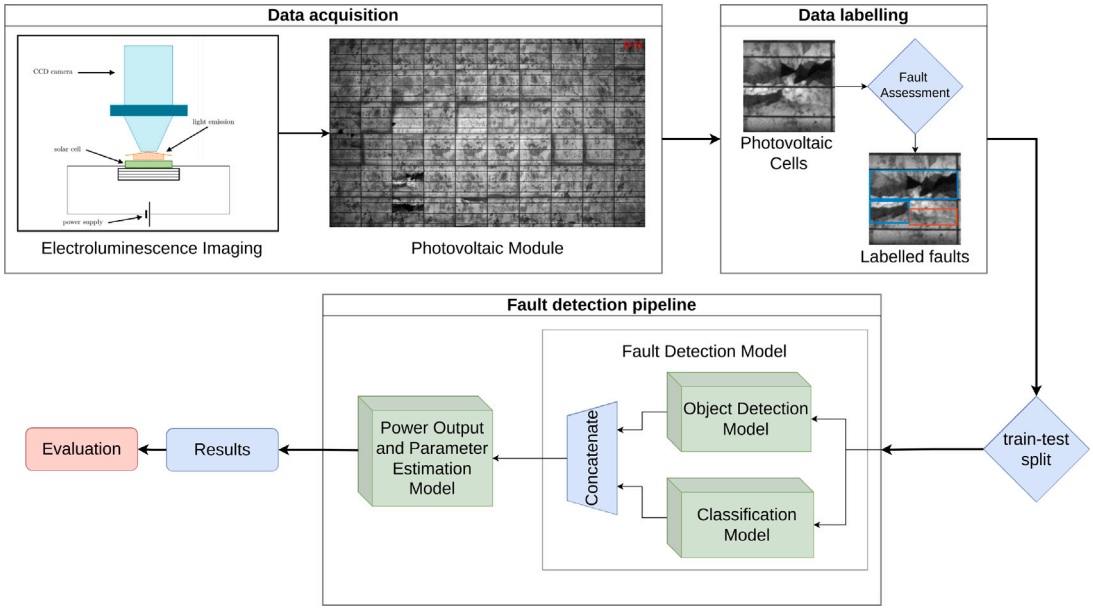

Fig. 7. The complete pipeline of the proposed methodology.

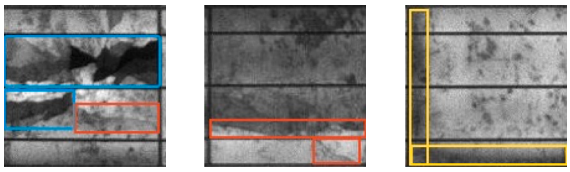

Fig. 8. Three different types of faults: (a) *black-core* fault (blue) and *crack* fault (orange), and *edge* fault (yellow).

the labeling process, which means small deviations during the labeling process might lead to an insufficient learning process. In the case of *crack* faults, the shape changes drastically depending on the process that led to the occurrence of cracks. Hence, in some images, cracks could span from edge to edge. This results in one bounding box which includes all the pixels in the image, including unnecessary information. This means that there will be other features in the bounding box that will affect the decisions of the ML model. Moreover, it is easy to overlook *crack* faults since trails of cracks are so complex that it is impossible to select all of them on some images, which introduces inconsistencies as mentioned before. Therefore, binary classification was used for *crack* faults.

Hence, there will be two types of labeling in this section:

1. For *black-core* and *edge* faults, use bounding boxes to identify the faults. Therefore, faults will have x and y coordinates in the EL image.
2. For *crack* faults, use binary classification of the EL image. Therefore, each image will have a "0" or "1" label in terms of cracks.

4.2. Train/validation splitting

Since the validation/test split should represent the whole dataset with unseen data, the partitioning was performed by considering the original fault distribution in the dataset by setting the random seed. Specifically, for each class, ±5% ratio difference was taken into account. Moreover, due to the small size of the dataset, the validation/test dataset was limited to 5 PV Modules (or 300 PV cell images). Hence, 24 PV modules for training and 5 for validation were used.

After splitting the data into train and validation sets, the train data flows into the fault detection model where the data is pre-processed. Then, it is used to train the object detection model and the classification model. The results of the fault detection model are evaluated on the validation data and the detected defects flow into the power output and series resistance estimation model. Similarly, the results are evaluated with the same validation data with different evaluation metrics, specific to the model's needs.

4.3. Utilized models

The DL pipeline consists of two models for two different purposes. Namely, detecting the faults in PV cells and estimating the power output and series resistance of PV modules. In this section, these two models will be presented in detail.

4.3.1. The fault detection model

Detecting faults requires two distinct models in parallel due to the labeling procedure. As mentioned before, bounding boxes have been used to label *black-core* and *edge* faults due to higher precision and accuracy even though the labeling process was challenging. Therefore, this leads to an object detection model. On the other hand, because of the challenges in detecting *crack* faults and its complex nature, binary classification was selected as labels. Hence, this leads to a classification model. The object detection and the classification model were combined to create the fault detection model, whose purpose is to detect the presence of any defects in PV cells.

Due to differences in labeling and nature of the each type of fault, pre-processing and post-processing will differ significantly from each other.

A. The object detection model

The fundamental reason behind using an object detection model to detect defects is to increase the model's ability to learn different types of faults from only one image. If a classification model was used, the model would need an extensive amount of data to understand the defects due to changes in defect types from image to image. To illustrate, if an image includes three *black-core* faults, the model will need at least three separate images that include only one of the similarly shaped defects. On the other hand, by limiting the fault area with a bounding box, the model will focus on important parts of the image and learn the shapes of the defects efficiently.

Moreover, another advantage of the object detection model is to examine the detections and fine-tune the labels to enhance the results.

The object detection model architecture is based on one of the most well-known models: YOLOv8 small [42]. YOLOv8, with its "anchor free" or no "prior boxes" design, aims to find the center points of the objects instead of focusing on the bounding boxes around the objects [42]. Therefore, it aims to decrease the bounding box distribution on the training dataset, where objects could be placed in the same place on the image. Due to its low number of parameters and being a one-stage detector, the YOLOv8 small model has achieved an mAP of 44.9 on the Microsoft COCO dataset [43] with 1.20 ms with A100 GPU [42].

A.1. Data pre-processing for the object detection model

Due to limited data size, it is important to increase the data size artificially. One of the most common methods is data augmentation (DA). DA allows us to increase the effective size of the dataset by applying simple transformations (such as adjusting brightness, and rotation) to the original dataset. However, it was observed that some DA methods negatively affected the observability of *black-core* and *edge* faults. To preserve the information regarding these faults, only horizontal and vertical random flipping were applied. Changing contrast, brightness, or clipping of the image could result in the loss of information in the data, therefore these methods were not used.

After DA, images were resized (640 by 640) due to the specific needs of YOLOv8, and the values of pixels were re-scaled to values between 1 and 0 by considering the original coordinates of bounding boxes.

A.2. Data post-processing for the object detection model

Post-processing was applied to the output estimations. Specifically, the process is as follows:

1. After the object detection model, results, which are coordinates and labels, of all the detected defects will be stored.
2. The coordinates and the number of detections for each defect will be filtered and each image will be classified by "0" or "1" for each type of defect.

B. The classification model

As mentioned before, using bounding boxes during labeling requires consistency. Due to the complex nature of *crack* defects, it is nearly impossible to label all cracks in a cell. Initial attempts regarding utilizing an object detection model to detect *crack* defects, resulted in poor accuracy and precision. Therefore, a classification model was used. As a result, a remarkable improvement in accuracy was observed.

The classification model architecture is based on MobileNetV2, which is light in terms of the number of parameters yet powerful due to inverted residual connections [44].

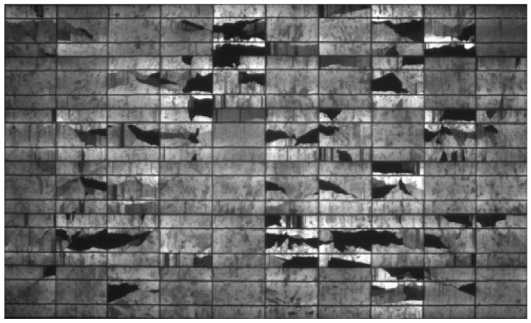

Fig. 9. 1-Channel image representation of a PV module (Module: "14414").

MobileNetV2 stands out from the crowd with its relatively high performance, 74.6% Top-1 accuracy, which means the estimation of the model with the highest probability is equal to the label, on ImageNet, compared to its number of parameters, 6.9M, thanks to inverted residual connections and linear bottlenecks [44]. Compared to the current state-of-the-art, Noisy Student (EfficientNet L2) which has achieved 88.41% on the ImageNet dataset with 480M parameters, by having only 6.9M parameters, MobileNetV2 has achieved a remarkable score and it is much easier to train on small datasets and deployable on smaller GPUs.

B.1. Data pre-processing for the classification model

Similarly, DA methods were applied to EL images in this case. Contrarily, in addition to random horizontal and vertical flipping, this time, random brightness was also applied, which did not affect *crack* faults negatively. After DA, the images were resized (128 by 128) to preserve the features of the original images (131 by 131), and the pixel values were re-scaled to values between 1 and 0.

4.3.2. The power output and parameter estimation model

The results of the fault detection model are used in the power output estimation model as the next step of the DL pipeline. At this step, the data is pre-processed and used to estimate the power output and series resistance in the equivalent circuit of the PV module.

A.1. Data pre-processing for the power output and parameter estimation model

Pre-processing in this part is fundamental. The pre-processing method will differ significantly for the candidate models according to the model's purpose but some steps are independent of the model's architecture:

- Images of the cells will be re-combined to create the corresponding PV panel image (Fig. 9).
- Similar to the cell images, defects will be combined to create the corresponding PV panel defect representation.

As presented in Section 3.2.2, in the equivalent circuit representation of the PV module, every two rows are in series and independent of the other rows due to by-pass diodes (Fig. 10). Therefore, while estimating the power output of the PV module, any defect in the grouped 20 PV cells will not affect the power output of the remaining PV cells.

Since the model does not know this higher-level information, the data should be pre-processed in such a way that the model should infer the independence of every two consecutive rows.

The proposed methodology is making the data 3-channel images. This idea stems from the fact that all images include three independent channels, each of which ranges from 1 to 255 real numbers or 0.0 to 1.0 as normalized values, except for the gray-scale images, which include only one channel. These three channels are, specifically, red (R), green

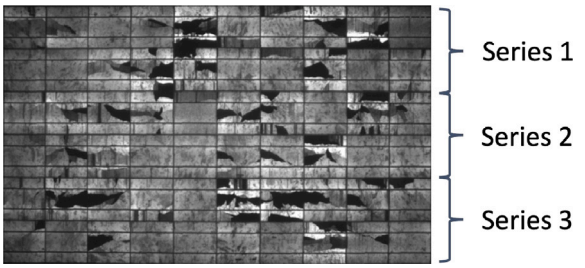

Fig. 10. PV module with series connection of cells (1310 by 1310 Image).

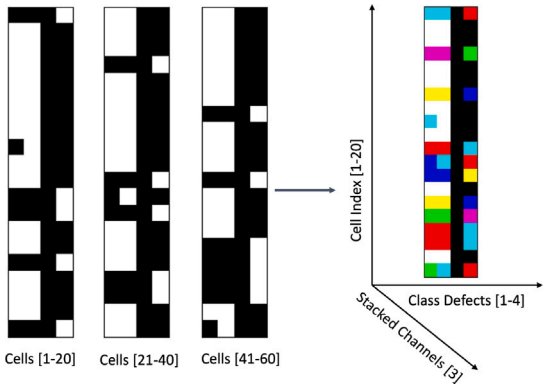

Fig. 11. Stacking the Defect Data Into 3-Channels (Module: "14414").

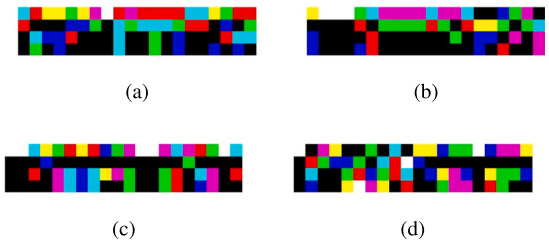

Fig. 12. Representation example for different tested PV Modules.

(G), and blue (B). To illustrate, for each pixel, as normalized values, R:1, G:1, B:1 results in white and R:0, G:0, B:0 results in black pixel.

In the PV modules, since there are six rows and every two rows are grouped, there are three independent groups, each of them consisting of 20 PV cells. Hence, there should be three independent channels in the images of PV modules. Therefore, one can embed the positions of cells together with the classification of the PV modules in these three channels (Fig. 11) as if they are colors so that the model understands that the information embedded in these channels is independent and results in a unique representation for each PV module (Fig. 12). This embedding results in the shape of 20 by 4 by 3, where the first number (20) stems from the number of cells in consecutive two rows that are connected by a single by-pass diode, the second number (4) results from the number of cell types (*black core*, *edge*, *crack*, and *empty*). The last number (3) corresponds to the image channel (RGB) in which the corresponding image slices are stacked.

Similar to the grouping process of defects in the PV cells, images of the PV cells could be grouped as well to represent the independence of every two consecutive rows in PV modules (Fig. 13). In addition to 3-channel data, 1-channel raw data, which was used in the existing studies, was used as a comparison as well so the effectiveness of this method can be observed (Fig. 9).

Furthermore, before training the power output estimation model, the true labels for the power output were normalized by 230 because

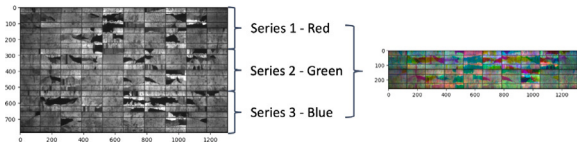

Fig. 13. 3-Channel image representation of a PV module (Module: "14414").

Table 4
Parameters of CNN-based power output estimation model.

CNN	Output Shape	Parameters
Input	20 x 4 x 3	0
Convolutional layer 1	19 x 3 x 128	1,664
Convolutional layer 2	18 x 2 x 64	32,832
Max pooling	9 x 1 x 64	0
Flatten	576	0
Output	1	577

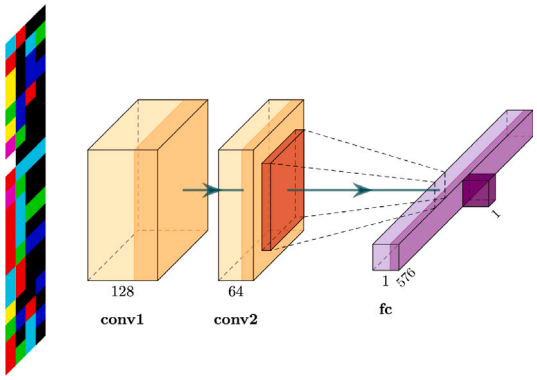

Fig. 14. Power output estimation model architecture.

of the rated power of the PV modules. Therefore, the results were normalized between 0.0 and 1.0, which will enable us to compare the results more accurately with the other studies since the comparison is in per-unit scale and independent from the rated power output of the PV module. On the other hand, even though in the dataset the maximum value that the true labels have is 0.9 for the series resistance, there is no limit to the value that the series resistance could have in the equivalent circuit representation. Hence, for the parameter estimation, the true labels will not be normalized as it was done in the power output estimation process. Instead, the errors will be normalized by the mean value of the true labels. Evaluation metrics will be demonstrated in Section 4.5 in detail.

A.2. The power and parameter estimation model architecture

The architecture of the proposed CNN-based power output and parameter estimation model can be seen in Table 4 and the visual representation with the PV module "14414" can be seen in Fig. 14.

4.4. Training

Training has been performed on Google Colab Pro instance with Nvidia V100 GPU and 64 GB RAM and TensorFlow version 2.14.

For all the models, to prevent over-fitting and increase the efficiency of the training process, callbacks were used:

1. Model checkpoint callback: To keep track of the lowest validation loss.
2. Reduce learning rate on plateau callback: The learning rate is multiplied by 0.5 if there is a plateau in terms of validation loss.
3. Early stopping callback: The training is interrupted if validation loss does not decrease for some epochs.

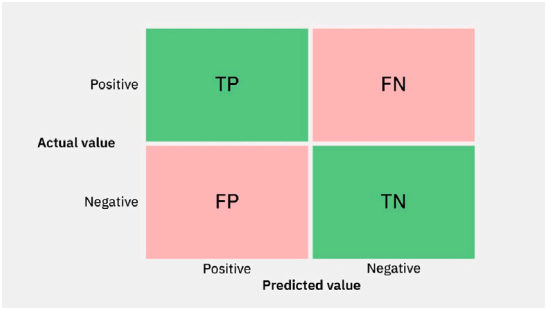

Fig. 15. Confusion matrix.

To validate the performance of the Power Output and Parameter Estimation model, a cross-validation technique was used. Specifically, the data was separated into 6-folds and fixed, where in each step train and validation data changed and the result was recorded. The number of folds (6) is selected to keep the ratio of the validation dataset sufficiently high (5 PV Modules) while ensuring the training dataset represents the original defect distribution. As a result, the mean of all results was found to determine the model's performance.

For the Object Detection and Classification models, cross-validation was not used. This is because of the high computational expense of the training procedure.

4.5. Evaluation metrics

4.5.1. Confusion matrix, accuracy, precision, and recall

The results of the binary classification problem could be represented on a 2 by 2 matrix where the values are the number of True Positives (TP), True Negatives (TN), False Positives (FP), and False Negatives (FN) [45]. This special matrix is called "confusion matrix" (Fig. 15).

Accuracy is the ratio of the correct classifications over all the examples in the dataset [46]. Accuracy measures how well a model performs in terms of correctly predicting class labels, which can be seen in Eq. (3).

$$Accuracy = \frac{\sum(TP + TN)}{\sum(TP + TN + FP + FN)} \tag{3}$$

Precision, also known as "confidence score", serves as a measure of how precise the detections are among all the positive predictions [46]. It quantifies the proportion of true positive detections (correctly identified objects) out of all the positive predictions and it is computed as in Eq. (4).

$$Precision = \frac{\sum TP}{\sum(TP + FP)} \tag{4}$$

Recall, computed as in Eq. (5), also known as "sensitivity", shows how sensitive the detections are out of all detections [46].

$$Recall = \frac{\sum TP}{\sum(TP + FN)} \tag{5}$$

4.5.2. Intersection over Union (IoU)

Intersection over Union (IoU) is a metric for algorithms such as object detection and image segmentation, whose purpose is to evaluate the ratio between the detected area and the true area of the object [47]. IoU quantifies the degree of overlap between two regions: the detected area (predicted bounding box or segmented region) and the true area (ground truth bounding box or annotated region). Hence, in Eq. (6), the numerator represents the overlapping region, while the denominator includes the union of the predicted (A) and true (B) areas.

$$IoU = \frac{area(A \cap B)}{area(A \cup B)} \tag{6}$$

It is important to mention that, IoU values range from 0 to 1 and according to COCO metrics [43], the minimum IoU threshold is 0.5. Therefore, detections lower than the threshold will be disregarded in terms of mean average precision, affecting the results negatively.

4.5.3. Mean Average Precision (mAP)

Average precision (AP) summarizes the precision–recall curve (PR-curve) by calculating the weighted mean of precisions achieved at each threshold [48]. The increase in recall at the previous threshold serves as the weight. Essentially, AP quantifies how well the model balances precision and recall across different confidence levels. As a result, a higher AP for each class indicates better detection accuracy and the mean of APs across all classes results in the mAP score. It is commonly used to evaluate object detection models.

4.5.4. Mean Absolute Error (MAE) and Root Mean Squared Error (RMSE)

Mean Absolute Error (MAE) is a useful measure that is being used widely for regression problems [49]. MAE quantifies the average absolute difference between the predicted values and the actual values in a dataset, as mathematically shown in Eq. (7). It gives the same importance to the farthest and the closest values from the predicted curve, which means MAE treats all errors equally, regardless of their magnitude. On the other hand, Root Mean Squared Error (RMSE), which can be computed as in Eq. (8), is the square root of the average squared difference between the predicted values and the actual values. It penalizes the farthest values, in other words, "outliers" from the ground truth are valued more. Therefore, it is a useful metric to analyze the robustness of the predictions [49].

$$MAE = \frac{1}{N}\sum_{i=1}^{N}\left|Y_i - \hat{Y}_i\right| \tag{7}$$

$$RMSE = \sqrt{\frac{1}{N}\sum_{i=1}^{N}\left|Y_i - \hat{Y}_i\right|^2} \tag{8}$$

A. Normalization for the power output estimation process

By normalizing the values Y_i and $\hat{Y}_i$, (in our case, normalized by the rated power, P_{rated} = 230 W, Eq. (9)) before calculating the metrics, the normalized versions of the metrics, nMAE (Eq. (10)) and nRMSE (Eq. (11)), can be found. They are commonly used to diminish the effect of units in estimation. Hence, the error will be between 0.0 and 1.0, which will allow the error to be compared with similar studies, regardless of the magnitude of the value being tried to estimate. Moreover, since the normalized error is between 0.0 and 1.0, the root value of the error will be larger. Therefore, nRMSE will represent the robustness of the predictions and the effect of outliers, as mentioned before. Ideally, these two error metrics should be equal to 0, but since it is nearly impossible, these metrics should be as close to 0 as possible.

$$y_i = \frac{Y_i}{P_{rated}} \quad \text{and} \quad \hat{y}_i = \frac{\hat{Y}_i}{P_{rated}} \tag{9}$$

$$nMAE_1 = \frac{1}{N}\sum_{i=1}^{N}\left|y_i - \hat{y}_i\right|, \tag{10}$$

$$nRMSE_1 = \sqrt{\frac{1}{N}\sum_{i=1}^{N}\left|y_i - \hat{y}_i\right|^2} \tag{11}$$

B. Normalization for the series resistance estimation process

As mentioned before, since there is no theoretical limit to the value that the resistance can take, normalization will be performed by the mean value of the true labels in the dataset. Therefore, changes can be seen in Eq. (12) and Eq. (13).

$$nMAE_2 = \frac{\frac{1}{N}\sum_{i=1}^{N}\left|Y_i - \hat{Y}_i\right|}{\bar{Y}}, \tag{12}$$

Table 5
Evaluation metrics for the proposed methodology.

Model	Metrics
Object Detection	mAP@0.50, AR@0.50-0.95
Classification	Accuracy, Precision, Recall, and F1 Score
Fault Detection	Accuracy, Precision, Recall, and F1 Score
Power Output and Parameter Estimation	nRMSE*, nMAE*; nRMSE**, nMAE**

* Normalization by the rated power P_{rated}.
** Normalization by the mean of the true labels.

$$nRMSE_2 = \frac{\sqrt{\frac{1}{N}\sum_{i=1}^{N}\left|Y_i - \hat{Y}_i\right|^2}}{\bar{Y}} \tag{13}$$

Where $\bar{Y}$ is the mean of Y

The evaluation metrics used to determine the performance of the models can be seen in Table 5.

5. Results

5.1. The fault detection model

To evaluate the performance of the fault detection model, the object detection and the classification model must be evaluated first.

A. The object detection model

The model was trained for 300 epochs and the training process was interrupted by the early stopping callback due to convergence. According to the results, the maximum $mAP@0.50 = 0.4561$ and $AR@0.50-0.95 = 0.5818$ was reached at epoch 184. To be able to comment on the results, some of the predictions of the object detection model should be examined.

In the first image in Fig. 16(a), even though the defect has been detected, the predicted area is much larger than the area of the label. According to the COCO metrics [43], this detection will be disregarded since the intersection over union (IoU) is smaller than 0.50. In Fig. 16(b), edge faults have been detected perfectly whereas one of the black core faults has not been detected since it is not obvious like the previous defects. In Fig. 16(c), the model caught the two faults almost perfectly.

B. The classification model

The model was trained for 50 epochs and the training process was interrupted by the early stopping callback due to convergence at epoch 44, similar to the previous model. At epoch 44, the accuracy is 86.80% and it is saved by the model checkpoint. To be able to comment on the results, some of the predictions of the classification model should be examined.

In Fig. 17, with cell "10474_3_2", the classification model struggles to detect the crack faults with no clear separation between the different sides. However, other cells are perfectly classified.

C. Results of the fault detection model

Since the true labels of each PV cell are known, evaluation metrics and confusion matrix for each type of fault can be calculated as in Fig. 18.

The detection results are promising across all fault types. Black core faults exhibit the most stability, likely due to the high prevalence of cells with these faults in the dataset. In the case of crack faults, the model shows significantly lower precision but higher recall compared to other metrics, indicating a high ratio of false positives and a high sensitivity to small changes in the images, which are often identified as cracks. For edge faults, while accuracy is notably high, both precision and recall are significantly lower. This discrepancy may stem from the relatively small number of PV cells with edge faults in the dataset.

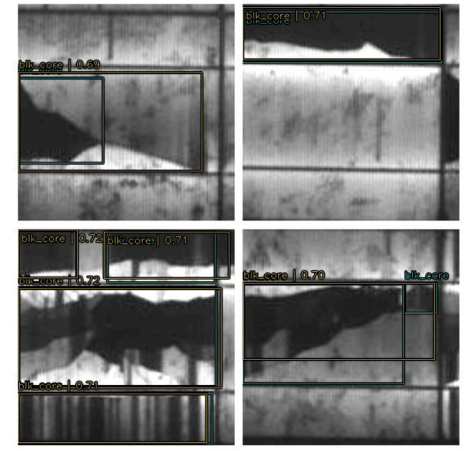

(a)

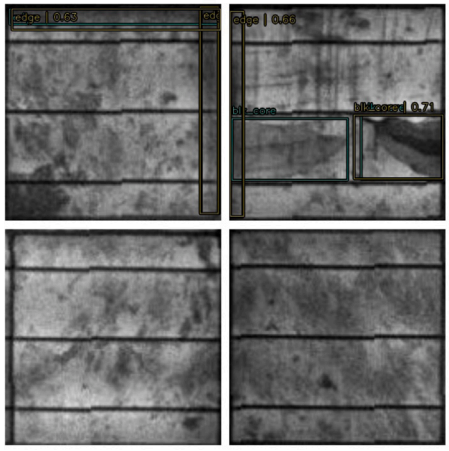

(b)

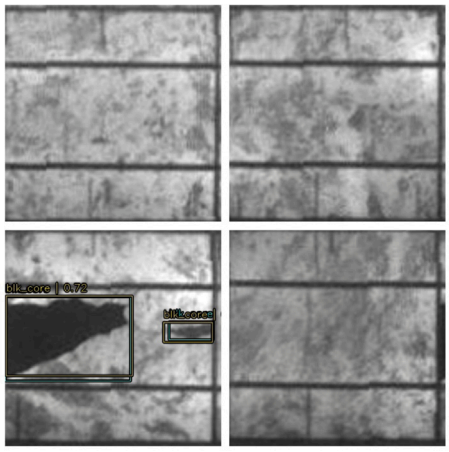

(c)

Fig. 16. Randomly chosen examples of detections of the Object Detection Model.

5.2. The power output and parameter estimation model

The best-performing model was selected using a 6-fold cross-validation technique from among seven candidate models. To assess the effectiveness of the proposed pre-processing technique proposed in the previous section, we first evaluated a baseline model that utilized only the 1-channel defect data, meaning there was no 3-channel stacking of the PV cells. Therefore, the proposed methodology was tested and validated.

Model name and the number of parameters of the candidate models can be seen in Table 6:

Table 6
Candidate models for the power output estimation model.

Model	Input Type	Parameters
Base	1-Channel Defects	241
3-Channel Defects Small	3-Channel Defects	1,664
3-Channel Defects Large*	3-Channel Defects	35,073
1-Channel Images**	1-Channel Image	1,057,025
1-Channel Images***	1-Channel Image	15,205,057
3-Channel Images**	3-Channel Images	371,585
Hybrid****	3-Channel Images and Defects	14,881,217

* Proposed model.
** Custom design CNN.
*** VGG16 based CNN.
**** VGG16 for images and custom design CNN for defects data.

A. Results of power output estimation

The results of nMAE and nRMSE errors for the 6-fold cross-validation can be seen in Fig. 19 and Fig. 20.

The base model, which uses only the 1-channel defect data, performs the worstan nMAE of 0.36339 and an nRMSE of 0.48871 since there is no higher-level information on the connection of PV cells within the PV module. On the other hand, the proposed model, "3-Channel Defects Large", performs the best with an nMAE of 0.03547 and an nRMSE of 0.04892 even though the number of parameters is significantly lower than the closest, the second best performing model, VGG16-based "1-Channel Images" which utilizes 1-channel raw EL images the PV modules similar to the existing studies. A smaller number of parameters means more efficient training and less inferring time for the model.

For the proposed model, not only nMAE error but also nRMSE is the lowest, suggesting that the outliers of the estimated power outputs are closer to the predicted regression line.

B. Results of series resistance estimation

The results of nMAE and nRMSE errors for the 6-fold cross-validation can be seen in Fig. 21 and Fig. 22.

Similar to the power output estimation result, the base model performs the worst with and nMAE of 0.49097 and an nRMSE of 0.60602, suggesting that the base model performs worse due to a lack of higher-level information on the connection of PV cells within the PV module. Regarding the best estimation, VGG16-based "1-Channel Images" performs significantly better than other candidate models, achieving an nMAE of 0.04472 and an nRMSE of 0.0622. In this case, the "3-Channel Defects Large" is the second-best performing model. These results suggest that a significantly larger model combined with the raw EL image of the PV modules is the best in terms of estimating the series resistance in the equivalent circuit compared to smaller models which contain a higher level of information regarding cell-level features.

6. Conclusions

This paper focuses on creating a complete DL pipeline that accomplishes three critical tasks: detecting faults within PV cells, estimating the power output of PV modules, and estimating the series resistance in the equivalent circuit representation of PV modules by analyzing the EL images. The first part of our pipeline is dedicated to detecting three types of faults within PV cells, namely *black-core*, *edge*, and *crack* faults. Due to the complexity of these faults, two different models for the fault detection process were employed, whose results are then combined.

The object detection model aims to detect *black-core* and *edge* faults within the PV cells with bounding boxes around them with the following details:

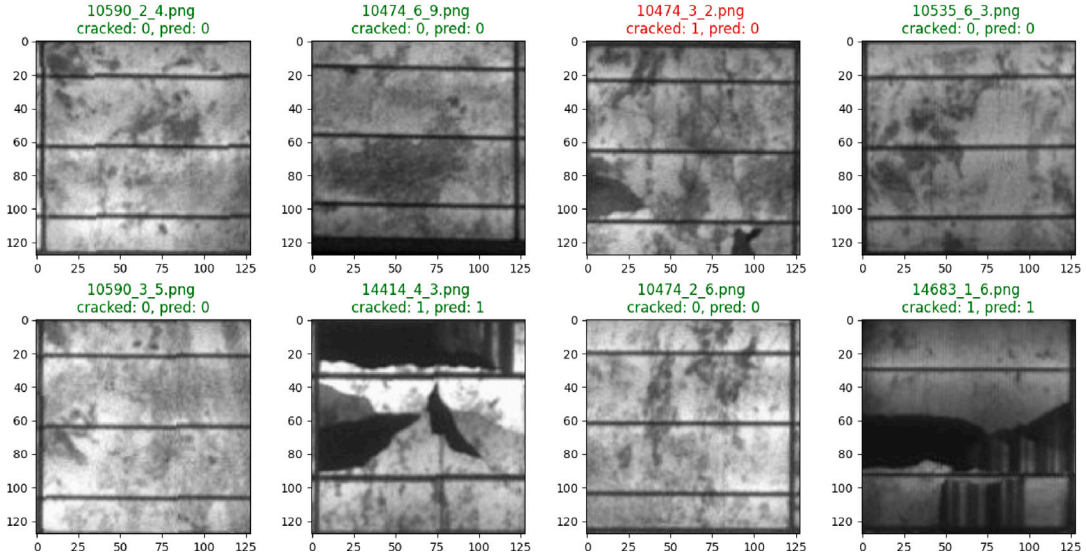

Fig. 17. Randomly chosen examples of detections of the Classification Model.

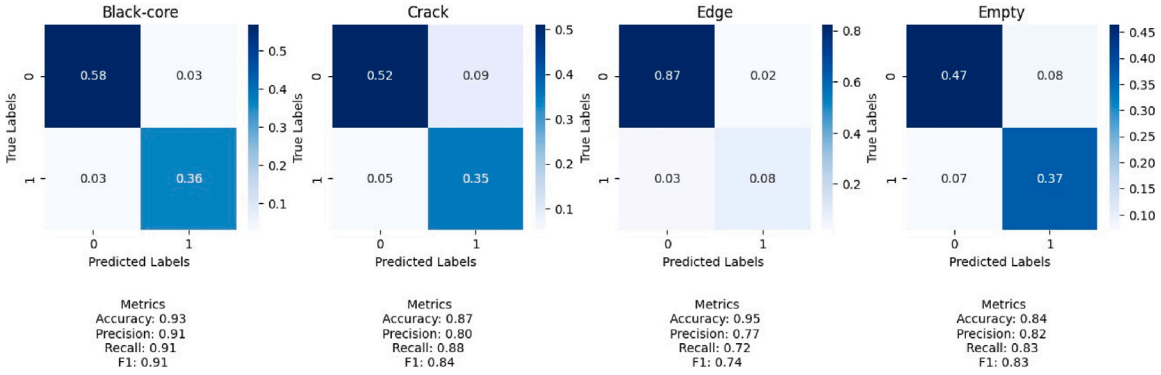

Fig. 18. Confusion matrix and evaluation results of the Fault Detection Model.

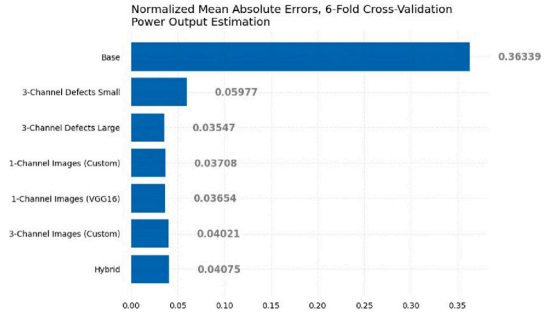

Fig. 19. Power Output Estimation, nMAE, 6-Fold Cross-validation.

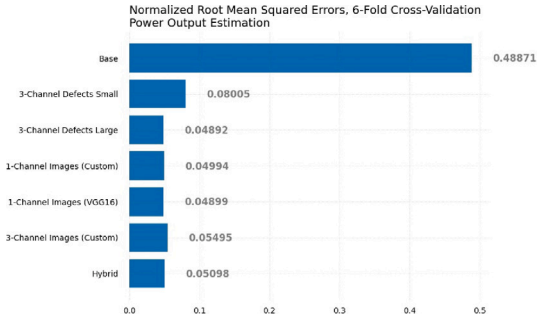

Fig. 20. Power Output Estimation, nRMSE, 6-Fold Cross-validation.

- The model specifically aims to identify *black-core* and *edge* faults within PV cells.
- The model provides bounding boxes with coordinates around these detected faults.
- The model achieves an mAP@0.50 of 0.4561 and an AR@0.50-0.95 of 0.5818.
- Since the number of detections per class is not required, the results are turned into binary values at the end.

The classification model for *crack* faults, in nature, produces binary values for the detections and can detect the faults with the following results:

- The model successfully detects *crack* faults with an accuracy of 0.868.

When the results of each model are concatenated and the results of the fault detection model are calculated, the fault detection model can detect faults with global accuracies:

- Black core: 0.93
- Crack: 0.868
- Edge: 0.95

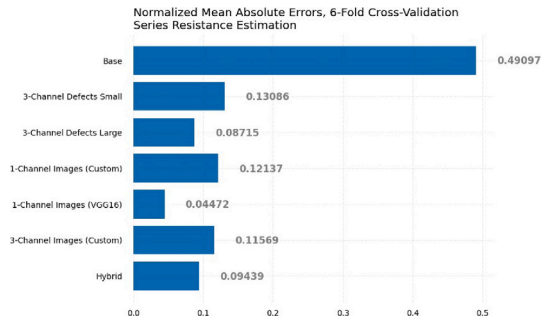

Fig. 21. Series Resistance, nMAE, 6-Fold Cross-validation.

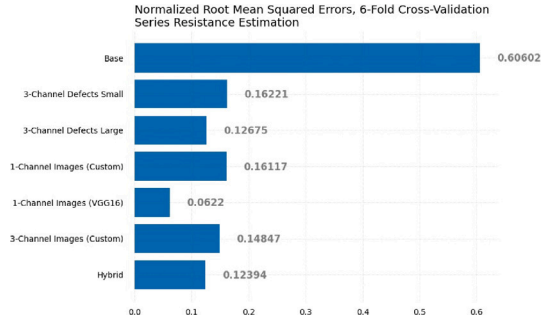

Fig. 22. Series Resistance Estimation, nRMSE, 6-Fold Cross-validation.

The results of the fault detection model are pre-processed in such a way that the connection of PV cells represents the equivalent circuit of the PV modules, where each pair of adjacent rows is separated by a diode, ensuring their independence in affecting the total power output.

To represent this situation, since there are six rows in PV modules, the defects data was embedded into a 3-channel representation, resulting in a unique RGB image for each PV module. These RGB images serve as a form of feature extraction and they were fed into a CNN-based power output and parameter estimation model, the second step of the DL pipeline. The proposed model with the extracted features, combined with the CNN model, outperforms the base model that relies solely on non-pre-processed detected faults, and larger models are significantly more adept at extracting features from EL images of PV modules in estimating the power output of the PV modules. The approach yields impressive results in terms of nMAE and nRMSE, as follows:

- nMAE: 0.03547
- nRMSE: 0.04892

Furthermore, the VGG16-based parameter estimation model was able to estimate the series resistance in the equivalent circuit representation of the PV modules by extracting features from the raw EL images of the PV modules with the following results:

- nMAE: 0.04472
- nRMSE: 0.0622

In summary, this paper showcases the effectiveness of using EL images to detect various types of faults within PV cells, estimate the output power of PV modules, and estimate the series resistance in the equivalent circuit representation of the PV modules. By combining extracted features with higher-level information about PV cells, standard approaches that rely solely on EL images of PV modules are surpassed. As a result, our findings contribute to advancing fault detection techniques, underscore the importance of considering cell-level features in PV technology, and bridge the gap between fault detection, power, and parameter estimation, leading to more accurate PV module performance assessments.

However, there are still some limitations of the applied methodology that could be more thoroughly investigated in future research. For instance, the estimation of output power and series resistance does not give a complete picture of the PV cell equivalent circuit. The second-stage model should be expended with a prediction of other important parameters, such as the shunt resistance. Moreover, EL images of PV modules used in this research are considerably difficult to acquire severely limiting a potential industry application of the proposed methodology. In future studies, similar research should be concluded that estimates the applicability of the applied techniques using images acquired in the visible spectrum which would allow for an easier and more efficient estimation of the well-being of PV cells.

CRediT authorship contribution statement

Emir Ozturk: Writing – original draft, Visualization, Software, Data curation. **Emanuele Ogliari:** Supervision, Methodology, Funding acquisition, Conceptualization. **Maciej Sakwa:** Writing – review & editing, Methodology, Investigation, Data curation, Conceptualization. **Alberto Dolara:** Validation, Supervision, Investigation. **Nicola Blasuttigh:** Validation, Data curation, Conceptualization. **Alessandro Massi Pavan:** Supervision, Resources, Investigation, Conceptualization.

Declaration of competing interest

The authors declare the following financial interests/personal relationships which may be considered as potential competing interests: Maciej Sakwa reports financial support was provided by European Union Next-GenerationEU. If there are other authors, they declare that they have no known competing financial interests or personal relationships that could have appeared to influence the work reported in this paper.

Data availability

The data that has been used is confidential.

Acknowledgments

This study was partly conducted within the Agritech National Research Center and received partial funding from the European Union Next-GenerationEU (PIANO NAZIONALE DI RIPRESA E RESILIENZA (PNRR) – MISSIONE 4 COMPONENTE 2, INVESTIMENTO 1.4 – D.D. 1032 17/06/2022, CN00000022). This manuscript reflects only the authors' views and opinions, neither the European Union nor the European Commission can be considered responsible for them. All authors have contributed equally. This work was supported in part by the "Ministero dell'Istruzione, dell'Università e della Ricerca" (Italy) under the Grant PRIN2020–HOTSPHOT 2020LB9TBC.

References

[1] Masson G, Bosch E, Rechem A, de l'Epine M, Kaizuka I, Jäger-Waldau A, et al. Snapshot of global PV markets 2023 task 1 strategic PV analysis and outreach PVPS. 2023.

[2] Sharma V, Chandel SS. Performance and degradation analysis for long term reliability of solar photovoltaic systems: A review. Renew Sustain Energy Rev 2013;27:753–67. http://dx.doi.org/10.1016/J.RSER.2013.07.046.

[3] Eitner U, Kajari-Schröder S, Köntges M, Altenbach H. Thermal stress and strain of solar cells in photovoltaic modules. In: Altenbach H, Eremeyev VA, editors. Shell-like structures: non-classical theories and applications. Berlin, Heidelberg: Springer Berlin Heidelberg; 2011, p. 453–68. http://dx.doi.org/10.1007/978-3-642-21855-2_29.

[4] Akram MW, Li G, Jin Y, Chen X. Failures of photovoltaic modules and their detection: A review. Appl Energy 2022;313:118822. http://dx.doi.org/10.1016/J.APENERGY.2022.118822.

[5] Niyaz HM, Meena R, Gupta R. Impact of cracks on crystalline silicon photovoltaic modules temperature distribution. Sol Energy 2021;225:148–61. http://dx.doi.org/10.1016/J.SOLENER.2021.07.038.

[6] Del Prado Santamaria R, Hass T, Benatto G, Ng J, Poulsen P, Spataru S. Machine aided estimation of solar cell crack caused power loss from electroluminescence images. In: Proceedings of 8th world conference on photovoltaic energy conversion. EU PVSEC; 2022, p. 480–7. http://dx.doi.org/10.4229/WCPEC-82022-3BO.11.6, 8th World Conference on Photovoltaic Energy Conversion, wcpec-8 ; Conference date: 26-09-2022 Through 30-09-2022, URL http://www.wcpec-8.com/.

[7] Köntges M, Siebert M, Morlier A, Illing R, Bessing N, Wegert F. Impact of transportation on silicon wafer-based photovoltaic modules. Prog Photovolt, Res Appl 2016;24:1085–95. http://dx.doi.org/10.1002/pip.2768.

[8] Köntges M. Review of failures of photovoltaic modules final - IEA-PVPS. 2021, URL https://iea-pvps.org/key-topics/review-of-failures-of-photovoltaic-modules-final/.

[9] Peshek TJ, Fada JS, Hu Y, Xu Y, Elsaeiti MA, Schnabel E, et al. Insights into metastability of photovoltaic materials at the mesoscale through massive I–V analytics. J Vac Sci Technol B, Nanotechnol Microelectron: Mater Process Measur Phenomena 2016;34. http://dx.doi.org/10.1116/1.4960628.

[10] Kumar V, Maheshwari P. Advanced analytics on IV curves and electroluminescence images of photovoltaic modules using machine learning algorithms. Prog Photovolt, Res Appl 2022;30:880–8. http://dx.doi.org/10.1002/pip.3469.

[11] Alves RHF, Júnior GAd, Marra EG, Lemos RP. Automatic fault classification in photovoltaic modules using convolutional neural networks. Renew Energy 2021;179:502–16. http://dx.doi.org/10.1016/J.RENENE.2021.07.070.

[12] Ksira Z, Mellit A, Blasuttigh N, Massi Pavan A. A novel embedded system for real-time fault diagnosis of photovoltaic modules. IEEE J Photovolt 2024;1–9. http://dx.doi.org/10.1109/JPHOTOV.2024.3359462.

[13] Jahn U. Review on IR and EL imaging for PV field applications - IEA-PVPS. 2020, URL https://iea-pvps.org/key-topics/review-on-ir-and-el-imaging-for-pv-field-applications/.

[14] Ramspeck K, Bothe K, Hinken D, Fischer B, Schmidt J, Brendel R. Recombination current and series resistance imaging of solar cells by combined luminescence and lock-in thermography. Appl Phys Lett 2007;90. http://dx.doi.org/10.1063/1.2721138.

[15] Frazão M, Silva JA, Lobato K, Serra JM. Electroluminescence of silicon solar cells using a consumer grade digital camera. Measurement 2017;99:7–12. http://dx.doi.org/10.1016/J.MEASUREMENT.2016.12.017.

[16] Deitsch S, Christlein V, Berger S, Buerhop-Lutz C, Maier A, Gallwitz F, et al. Automatic classification of defective photovoltaic module cells in electroluminescence images. Sol Energy 2019;185:455–68. http://dx.doi.org/10.1016/J.SOLENER.2019.02.067.

[17] Doll B, Hepp J, Hoffmann M, Schuler R, Buerhop-Lutz C, Peters IM, et al. Photoluminescence for defect detection on full-sized photovoltaic modules. IEEE J Photovolt 2021;11:1419–29. http://dx.doi.org/10.1109/JPHOTOV.2021.3099739.

[18] Manno D, Cipriani G, Ciulla G, Di Dio V, Guarino S, Lo Brano V. Deep learning strategies for automatic fault diagnosis in photovoltaic systems by thermographic images. Energy Convers Manage 2021;241:114315. http://dx.doi.org/10.1016/j.enconman.2021.114315, URL https://www.sciencedirect.com/science/article/pii/S019689042100491X.

[19] Jeffrey Kuo C-F, Chen S-H, Huang C-Y. Automatic detection, classification and localization of defects in large photovoltaic plants using unmanned aerial vehicles (UAV) based infrared (IR) and RGB imaging. Energy Convers Manage 2023;276:116495. http://dx.doi.org/10.1016/j.enconman.2022.116495, URL https://www.sciencedirect.com/science/article/pii/S0196890422012730.

[20] Mellit A, Blasuttigh N, Pavan AM. TinyML for fault diagnosis of Photovoltaic Modules using Edge Impulse Platform. In: 2023 11th international conference on smart grid (icSmartGrid). 2023, p. 01–5. http://dx.doi.org/10.1109/icSmartGrid58556.2023.10171088.

[21] Ksira Z, Blasuttigh N, Mellit A, Pavan AM. TinyML model for fault classification of photovoltaic modules based on visible images. In: IoT-enabled energy efficiency assessment of renewable energy systems and micro-grids in smart cities. vol. 984, Cham: Springer Nature Switzerland; 2024, p. 373–80. http://dx.doi.org/10.1007/978-3-031-60629-8_37, Series Title: Lecture Notes in Networks and Systems, URL https://link.springer.com/10.1007/978-3-031-60629-8_37.

[22] Krizhevsky A, Sutskever I, Hinton GE. ImageNet classification with deep convolutional neural networks. Commun ACM 2017;60:84–90. http://dx.doi.org/10.1145/3065386.

[23] Simonyan K, Zisserman A. Very deep convolutional networks for large-scale image recognition. 2014.

[24] He K, Zhang X, Ren S, Sun J. Deep residual learning for image recognition. 2015.

[25] Redmon J, Divvala S, Girshick R, Farhadi A. You only look once: Unified, real-time object detection. 2015.

[26] Akram MW, Li G, Jin Y, Chen X, Zhu C, Zhao X, et al. CNN based automatic detection of photovoltaic cell defects in electroluminescence images. Energy 2019;189:116319. http://dx.doi.org/10.1016/J.ENERGY.2019.116319.

[27] Demirci MY, Beşli N, Gümüşçü A. Efficient deep feature extraction and classification for identifying defective photovoltaic module cells in electroluminescence images. Expert Syst Appl 2021;175:114810. http://dx.doi.org/10.1016/J.ESWA.2021.114810.

[28] Et-taleby A, Chaibi Y, Allouhi A, Boussetta M, Benslimane M. A combined convolutional neural network model and support vector machine technique for fault detection and classification based on electroluminescence images of photovoltaic modules. Sustain Energy Grids Netw 2022;32:100946. http://dx.doi.org/10.1016/J.SEGAN.2022.100946.

[29] Karimi AM, Fada JS, Hossain MA, Yang S, Peshek TJ, Braid JL, et al. Automated pipeline for photovoltaic module electroluminescence image processing and degradation feature classification. IEEE J Photovolt 2019;9:1324–35. http://dx.doi.org/10.1109/JPHOTOV.2019.2920732.

[30] Chen X, Karin T, Jain A. Automated defect identification in electroluminescence images of solar modules. Sol Energy 2022;242:20–9. http://dx.doi.org/10.1016/J.SOLENER.2022.06.031.

[31] Tang W, Yang Q, Xiong K, Yan W. Deep learning based automatic defect identification of photovoltaic module using electroluminescence images. Sol Energy 2020;201:453–60. http://dx.doi.org/10.1016/J.SOLENER.2020.03.049.

[32] Zhao X, Song C, Zhang H, Sun X, Zhao J. HRNet-based automatic identification of photovoltaic module defects using electroluminescence images. Energy 2023;267:126605. http://dx.doi.org/10.1016/j.energy.2022.126605, URL https://linkinghub.elsevier.com/retrieve/pii/S0360544222034922.

[33] Zhang X, Hao Y, Shangguan H, Zhang P, Wang A. Detection of surface defects on solar cells by fusing multi-channel convolution neural networks. Infrared Phys Technol 2020;108:103334. http://dx.doi.org/10.1016/J.INFRARED.2020.103334.

[34] Zhao Y, Zhan K, Wang Z, Shen W. Deep learning-based automatic detection of multitype defects in photovoltaic modules and application in real production line. Prog Photovolt, Res Appl 2021;29:471–84. http://dx.doi.org/10.1002/pip.3395, URL https://onlinelibrary.wiley.com/doi/10.1002/pip.3395.

[35] Meng Z, Xu S, Wang L, Gong Y, Zhang X, Zhao Y. Defect object detection algorithm for electroluminescence image defects of photovoltaic modules based on deep learning. Energy Sci Eng 2022;10:800–13. http://dx.doi.org/10.1002/ese3.1056, URL https://onlinelibrary.wiley.com/doi/10.1002/ese3.1056.

[36] Otamendi U, Martinez I, Quartulli M, Olaizola IG, Viles E, Cambarau W. Segmentation of cell-level anomalies in electroluminescence images of photovoltaic modules. Sol Energy 2021;220:914–26. http://dx.doi.org/10.1016/J.SOLENER.2021.03.058.

[37] Fioresi J, Colvin DJ, Frota R, Gupta R, Li M, Seigneur HP, et al. Automated defect detection and localization in photovoltaic cells using semantic segmentation of electroluminescence images. IEEE J Photovolt 2022;12:53–61. http://dx.doi.org/10.1109/JPHOTOV.2021.3131059, URL https://ieeexplore.ieee.org/document/9650542/.

[38] Hoffmann M, Buerhop-Lutz C, Reeb L, Pickel T, Winkler T, Doll B, et al. Deep learning-based pipeline for module power prediction from EL measurements. 2020, URL http://arxiv.org/abs/2009.14712.

[39] Karimi AM, Fada JS, Parrilla NA, Pierce BG, Koyuturk M, French RH, et al. Generalized and mechanistic PV module performance prediction from computer vision and machine learning on electroluminescence images. IEEE J Photovolt 2020;10:878–87. http://dx.doi.org/10.1109/JPHOTOV.2020.2973448.

[40] Battaglia M, Comi E, Stadelmann T, Hiestand R, Ruhstaller B, Knapp E. Deep ensemble inverse model for image-based estimation of solar cell parameters. APL Mach Learn 2023;1. http://dx.doi.org/10.1063/5.0139707, URL https://pubs.aip.org/aml/article/1/3/036108/2904738/Deep-ensemble-inverse-model-for-image-based.

[41] De Soto W, Klein S, Beckman W. Improvement and validation of a model for photovoltaic array performance. Sol Energy 2006;80(1):78–88. http://dx.doi.org/10.1016/j.solener.2005.06.010, URL https://www.sciencedirect.com/science/article/pii/S0038092X05002410.

[42] Jocher G, Chaurasia A, Qiu J. Ultralytics YOLO. 2023, URL https://github.com/ultralytics/ultralytics.

[43] Lin T-Y, Maire M, Belongie S, Bourdev L, Girshick R, Hays J, et al. Microsoft COCO: Common objects in context. 2014.

[44] Sandler M, Howard A, Zhu M, Zhmoginov A, Chen L-C. MobileNetV2: Inverted residuals and linear bottlenecks. 2018.

[45] Powers DMW. Evaluation: from precision, recall and F-measure to ROC, informedness, markedness and correlation. 2020, arXiv:2010.16061.

[46] Everingham M, Gool LV, Williams CKI, Winn J, Zisserman A. The pascal visual object classes (VOC) challenge. Int J Comput Vis 2010;88:303–38. http://dx.doi.org/10.1007/s11263-009-0275-4.

[47] Rahman M, Wang Y. Optimizing intersection-over-union in deep neural networks for image segmentation. In: International symposium on visual computing. 2016, URL https://api.semanticscholar.org/CorpusID:11243044.

[48] Henderson P, Ferrari V. End-to-end training of object class detectors for mean average precision. In: Lai S-H, Lepetit V, Nishino K, Sato Y, editors. Computer vision – ACCV 2016. Cham: Springer International Publishing; 2017, p. 198–213.

[49] Chai T, Draxler RR. Root mean square error (RMSE) or mean absolute error (MAE). Geosci Model Dev Dis 2014;7(1):1525–34.